

Original Paper

Quantitative Analysis of Micro-structural Changes in a Bituminous Coal After Exposure to Supercritical CO₂ and Water

Guanglei Zhang,¹ P. G. Ranjith ,^{1,4} M. S. A. Perera,^{1,2} Yiyu Lu,³ and Xavier Choi¹

Received 11 November 2018; accepted 23 January 2019

Published online: 31 January 2019

High-volatile bituminous coal samples were reacted in deionized water with supercritical CO₂ (ScCO₂-water) under simulated in situ pressure and temperature conditions (8 MPa and 40 °C) in unconfined stress state for 14 days, in order to characterize potential CO₂-water-coal reactions. Micro-structural changes were identified pre- and post-experiment using X-ray powder diffraction (XRD) analysis for powdered coal (mineralogical changes), optical microscopy and scanning electron microscopy (SEM) for polished thin sections (surface feature changes) and micro-CT scanning for a small core (porosity and permeability changes). XRD analysis revealed that carbonic acid leaches out mineral matters in coal, including carbonates (calcite) and silicate minerals (albite, illite and kaolinite). Optical microscopy, SEM and CT images confirmed that the interaction of coal with ScCO₂-water causes an abundance of micro-cracks to open or propagate in unconfined coal samples. Most micro-cracks preferably propagated along maceral-mineral and maceral-maceral interfaces, which demonstrates that the micro-cracking was caused by differential swelling of different coal lithotypes. Wormhole formation was observed in coal caused by mineral dissolution and hydrocarbon mobilization, which significantly increases coal porosity compared with swelling-induced cracking. 3-D pore network models extracted from CT images show that ScCO₂-water treatment enlarges the pore and throat size, increases the numbers of pores and throats and improves pore network connectivity. Overall, CO₂-water-coal interactions under unconfined conditions enhance coal porosity, connectivity and permeability, which can be attributed to the combined effect of micro-cracking, mineral dissolution and hydrocarbon mobilization.

KEY WORDS: Supercritical CO₂, Micro-CT, Pore network model, Connectivity.

INTRODUCTION

Carbon dioxide (CO₂) sequestration in deep unmineable coal seams has been identified as a promising technology to mitigate CO₂ emissions and has the additional benefit of enhancing coalbed methane (CBM) recovery (CO₂-ECBM) (White et al. 2005; Anderson 2017a, b). Successful implementation of CO₂ sequestration in coal seams relies on a full understanding of the interactions between coal and CO₂ under in situ conditions. Since the preferred coal seams for CO₂ sequestration are lo-

¹Deep Earth Energy Laboratory, Department of Civil Engineering, Monash University, Building 60, Melbourne, VIC 3800, Australia.

²Department of Infrastructure Engineering, The University of Melbourne, Building 176, Melbourne, VIC 3010, Australia.

³State Key Laboratory of Coal Mine Disaster Dynamics and Control, Chongqing University, Chongqing 400044, China.

⁴To whom correspondence should be addressed; e-mail: ranjith.pg@monash.edu

cated at great depths (> 800 m), CO_2 exists in a supercritical state under in situ pressure and temperature regime, exhibiting complex physical properties of both gas and liquid (Perera et al. 2011a, b). In addition, although coal seams for CBM production have been mostly dewatered, there is still formation water left in the seams. After injection of CO_2 , supercritical CO_2 (ScCO_2) and water mixture interact with both organic and inorganic matters in coal and change coal's micro-structure in at least three ways. Firstly, CO_2 molecules have great affinity to coal and are not only adsorbed on the coal surface, but also dissolve into coal organic matters. This process modifies coal's physical structure. Larsen (2004) suggested that CO_2 acts as a plasticizer, causing coal's macromolecular structure re-arrangement, which swells coal. Coal swelling is a highly heterogeneous process depending on the lithotypes present, and vitrinite has high degree of swelling compared to clay minerals and inertinite (Karacan 2007). As a result, the volumetric strains of coal are associated with both swelling and compression, depending on the lithotypes and locations. Coal swelling is also CO_2 pressure-dependent and coal rank-dependent (Reucroft and Sethuraman 1987, Karacan 2007; Day et al. 2008). Secondly, ScCO_2 also has great ability to extract some polycyclic aromatic hydrocarbons and mobilize them in coalbeds, called the hydrocarbon mobilization effect. Substantial hydrocarbon leaching with ScCO_2 has been reported (Kolak and Burruss 2006; Mazumder et al. 2006; Zhang et al. 2013), and this also changes the physical properties of coal. Thirdly, similar to CO_2 sequestration in deep saline aquifers, carbonic acid forms after CO_2 injection and causes mineral dissolution, resulting in the alteration of porosity, pore space connectivity and permeability (Wigand et al. 2008; Yu et al. 2012; Farquhar et al. 2015; Wang et al. 2016).

The interaction between ScCO_2 , formation water and coal (ScCO_2 -water-coal) leads to physical and chemical changes in coal seams, which eventually cause changes in the reservoir properties. Field and experimental studies have shown that ScCO_2 leads to volumetric swelling of coals, and the resultant permeability reduction has been widely reported (Mazumder and Wolf 2008; Fujioka et al. 2010; Pan et al. 2010). The research group of the second author of this paper has carried out a series of uni-axial and tri-axial compression tests on different rank coals after reaction with ScCO_2 , and has found that the strength and elastic modulus of coal

significantly reduce irrespective of coal rank (Viete and Ranjith 2006; Perera et al. 2011a, b; Perera et al. 2013; Ranathunga et al. 2016a, b; Zhang et al. 2019). A number of studies have also been concerned with changes in the pore structure of coal after exposure to ScCO_2 or a mixture of ScCO_2 and water using different types of analytical methods (Zhou et al. 2017): (1) fluid injection techniques, including helium pycnometry, mercury porosimetry and N_2/CO_2 adsorption (Gathitu et al. 2009; Massarotto et al. 2010; Zhang et al. 2013, 2017); (2) microscopic imaging techniques, such as scanning electron microscopy and optical microscopy (Gathitu et al. 2009; Kutchko et al. 2013; Meng and Qiu 2018; Dong et al. 2019); and (3) nondestructive physical techniques, such as nuclear magnetic resonance (Li et al. 2017). To date, many researchers have combined two or more methods to study the pore morphology and have drawn the conclusion that $\text{ScCO}_2/\text{ScCO}_2$ -water treatment changes the pore volume, pore size distribution, pore shape and connectivity of coal. However, these methods can only quantify the pore structure change but shed little light on the 3-D fracture network change of coal. In the CO_2 -ECBM process, the injected CO_2 flows through the fracture network and adsorbs on the pore surface in the coal matrix. The size and connectivity of the fracture network control coal permeability, which is essential for evaluating the feasibility and efficiency of sequestration projects. Recently, X-ray computed tomography (CT) techniques have been used in coal research (Zhang et al. 2016a; Mathews et al. 2017), which present the opportunity to accurately present the coal fracture network of coal.

In this paper, we focus on the quantitative analysis of the fracture network change of coal using X-ray CT scanning and we then quantify the resultant fracture porosity and permeability change after exposure to ScCO_2 -water. X-ray powder diffraction (XRD) analysis provides evidence for mineralogical changes in coal, and optical microscopy and scanning electron microscopy (SEM) give information about changes to the 2-D surface features of coal.

MATERIALS AND METHODS

Coal Samples

The coal was high-volatile bituminous collected from the Tashan coal mine, in Shanxi province, China. Proximate analysis was performed on a sister

core of the sample according to the Chinese Standard (GB/T212-2001) and a summary of the sample proximate analysis is provided in Table 1. We calculated sample porosity experimentally by water saturation. Dry samples were saturated with water for more than 1 month to ensure all the pores in samples were filled. The measured porosity was 5.13% by calculating the weight difference between saturated and dry samples.

The samples used for this study were extracted from the same coal block (Fig. 1). A cylinder samples (38 mm in diameter, ~ 20 mm in length) drilled out of the block was used for 3-D X-ray micro-CT scanning. Small, rough-cut and polished thin sections, measuring approximately 5 mm × 5 mm × 3 mm, were taken from adjacent places in the same block for 2-D optical microscopy and SEM. Bulk coal samples were finely ground in an agate mortar and sieved to 15 microns for quantitative XRD measurement.

To assess the effect of ScCO₂-water saturation, all samples for 2-D and 3-D imaging were first scanned in their initial state and then characterized again after interaction. In addition, the coal powders were divided into two equal parts. One part was used as a reference sample and the other part was saturated under the same conditions as the cylinder

and thin sections. Both powders were analyzed and compared using XRD to assess the mineral change.

ScCO₂-Water Saturation

The experiments were conducted in a reaction chamber (Fig. 2) comprising a reaction vessel 60 mm in diameter and 100 mm deep equipped with an electronic heating jacket. CO₂ was injected using an ISCO syringe pump and the pressure was measured using a pressure gauge. A heating jacket was wrapped around the chamber, and the temperature was maintained by a thermocouple. Prior to commencing the CO₂ injection, whole samples were fully submerged in deionized water at 40 °C for 2 h. Later, ScCO₂ was introduced into the reactor to full pressure (8 MPa). The experimental conditions of injection pressure *P* and temperature *T* were chosen to be within the CO₂ supercritical condition, and the samples were allowed to react for 14 days with the ScCO₂-water mixture. The experiment duration chosen is sufficient to reach the reaction equilibrium of the experiment (Liu et al. 2018). After exposure, the chamber was depressurized slowly to avoid any potential damage induced by a sudden change in pressure.

Table 1. Results of proximate analysis

IM (wt%)	Ash (wt%)	VM (wt%)	FC (wt%)
1.31	13.16	25.72	59.81

IM inherent moisture, *VM* volatile matter, *FC* fixed carbon

Analytical Techniques

To characterize the micro-structural change of coal after ScCO₂-water exposure, different analytical methods, including XRD, optical microscopy, SEM and micro-CT, were used to reveal the effects



Figure 1. Sampling strategy for ScCO₂-water saturation experiments and micro-structural characterization.

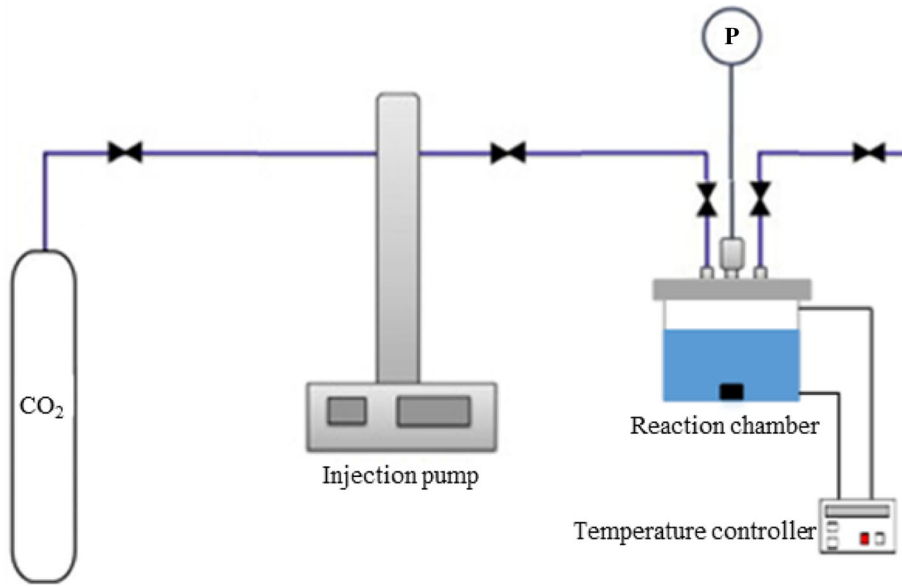


Figure 2. Schematic of high-pressure and high-temperature setup for ScCO₂-water-coal experiment. The supercritical gas phase exists above the deionized water (shown in blue) containing saturated samples.

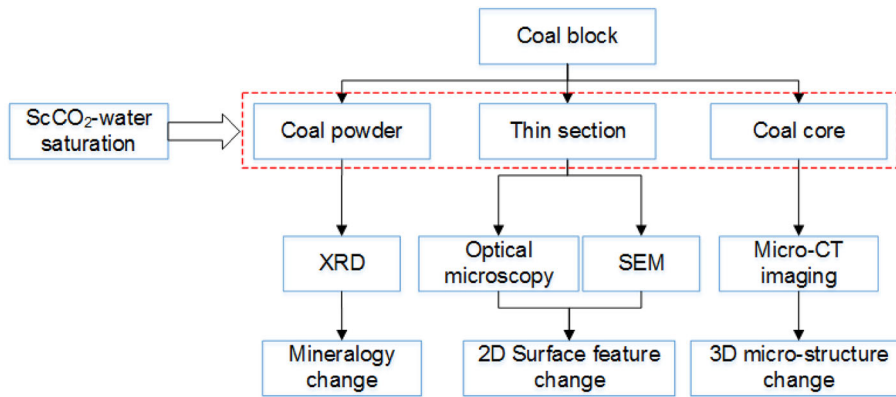


Figure 3. Flowchart of analytical methods used in this study.

of ScCO₂ on the alteration of the physicochemical properties of coal (refer to Fig. 3).

XRD

The mineral composition of the reacted samples was determined using XRD at Monash University. A Bruker D8 advance device was used with CuKα radiation at 40 mA and 40 kV. The measurements were carried out in a 2θ range of 5° to 60° with a step size of 0.01° and a scanning speed of 0.5 s/step.

Quantification phase analysis was conducted with the Rietveld method using TOPAS 5.0 (Bruker).

Optical Microscopy and SEM Analysis

Optical microscopy and SEM observations allow us to image nanometer-scale structural change after ScCO₂-water saturation. Optical microscopy and SEM analysis were carried out using a Nikon Eclipse Ni optical microscope and a FEI Quanta 3D FEGSEM, respectively. SEM pictures were taken in

both secondary electron imaging mode and backscatter electron imaging mode.

Micro-CT Imaging

X-ray micro-CT imaging using a monochromatic X-ray beam was carried out at hutch 3B of the Australian Synchrotron's Imaging and Medical beamline. The scanning parameters used in this study are listed in Table 2. The pixel size of the CT images was 17.8 μm . Reconstruction of the tomographic data was done using X-TRACT software, and the reconstructed data were further analyzed using the Avizo 9.0 package. All the image reconstruction and processing process were run on the MASSIVE supercomputer cluster, which enabled a large number of datasets to be reconstructed

Table 2. Scanning parameters of IMBL beamline used in this study

Scanning parameters	Specifications
Acquisition time	20 min
X-ray energy	60 keV
Detector	Ruby with 150 mm lens and 20 μm scintillator
Detector-to-sample distance	0.4 m
Total number of projections	1800 projections

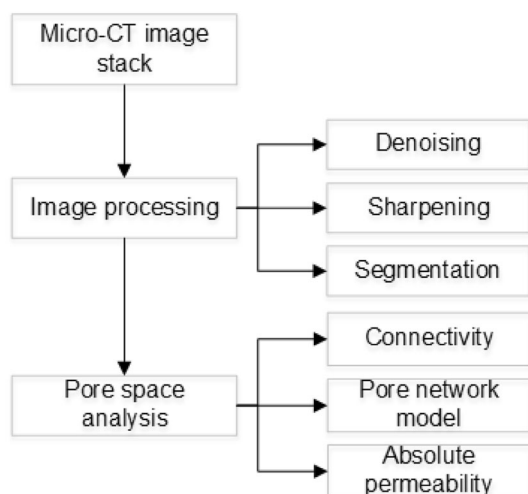


Figure 4. Schematic diagram of workflow for image processing and analysis.

quickly. Figure 4 shows the typical workflow for image processing and analysis.

Image Processing. This was comprised by the following main steps. CT images were first de-noised using the anisotropic diffusion filter and un-sharp masking was then used to enhance the contrasts at the edges between different phases. Next, watershed-based segmentation was adopted to accurately segment the coal matrix, minerals and fractures in the coal (Andrew et al. 2013; Taylor et al. 2015). Details of the image processing and segmentation procedures can be found in Zhang et al. (2018a, b).

Pore Space Analysis. A preliminary connectivity test was performed prior to the permeability computation or pore network model extraction in order to remove isolated pores that contribute little to fluid flow. The connectivity analysis was done by considering 6-neighborhood connectivity: flow can only move from one voxel to the adjacent voxel through one of the voxel faces. Only pore spaces connected to each other were labeled as connected porosity. The lattice Boltzmann method (LBM) was then adopted to calculate the absolute permeability on the connected pore spaces. In the LBM method, fluids can be imagined as consisting of small particles which undergo particle 'streaming' and 'collision' (Shan and Chen 1993; He and Luo 1997). This process can be simulated by the Boltzmann transport equation. A detailed description of permeability simulation using LBM and verification using experimental results can be found in Zhang et al. (2018a, b).

Pore network models (PNMs) have been found to be a valuable tool for understanding the topological characteristics and transport properties of pore structures (Blunt 2001). In PNM framework, the complex pore space can be simplified as an equivalent network where relatively large pore bodies at the nodes of the network are connected by smaller pore throats (Dong et al. 2008). In this way, the network topological parameters (e.g., aspect ratio, connectivity and tortuosity) are considered in the model (De Boever et al. 2012). The critical part in the PNM extraction process is the precise identification of the topological skeleton, i.e., the pore bodies and throats. The detailed algorithm is described in Zhang et al. (2018a, b). The extraction of the PNM allows comprehensive pore network attributes to be obtained, including the pore/throat ra-

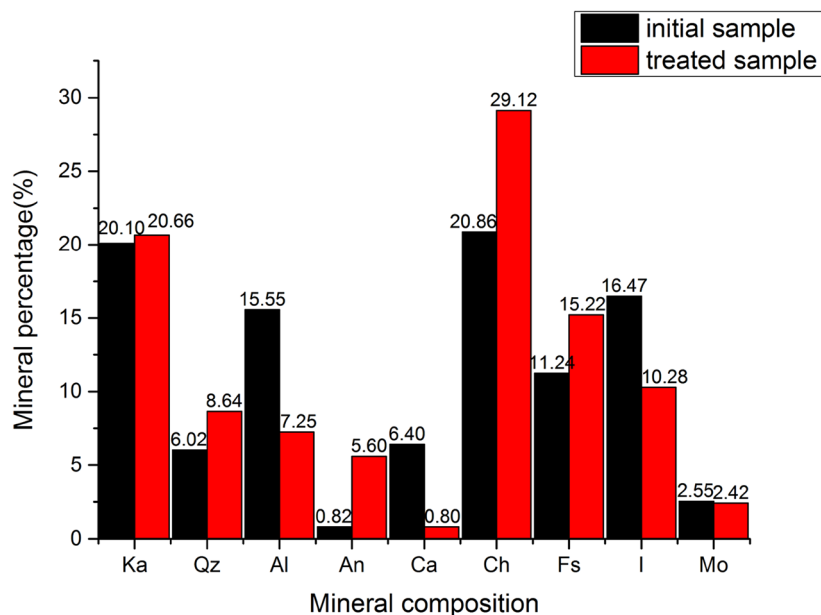


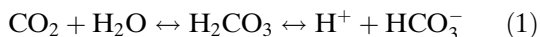
Figure 5. Mineralogical change of coal powder after ScCO₂-water treatment. Ka, I, Ch, Fs, Qz, Al, An, Ca, and Mo represent kaolinite, illite, chlorite, feldspar, quartz, albite, analcime, calcite and montmorillonite, respectively.

dus, pore coordination number, pore volume and throat channel length.

RESULTS AND DISCUSSION

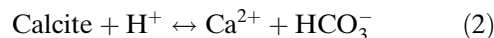
Mineralogical Change

XRD semiquantitative analysis confirmed that the mineral composition of the sample includes chlorite, kaolinite, illite, albite, feldspar, quartz, calcite, montmorillonite and analcime. CO₂ is reactive gas that can cause mineral dissolution and precipitation. After injection, CO₂ dissolves in formation water and carbonic acid (H₂CO₃) forms (Eq. 1):



This results in a decrease in pH, which in turn causes mineral dissolution and ion release from the mineral surface (Apps et al. 2010; Farquhar et al. 2015). Previous studies have confirmed that the CO₂-brine-rock interaction can cause the dissolution of carbonate and silicate minerals and the formation of new minerals. However, the results vary with different researchers as the heterogeneity of

different rock samples used in different experiments differs. Wigand et al. (2008) observed the dissolution of dolomite cement, K-feldspar and albite and the formation of montmorillonite in sandstone after saturation with ScCO₂. Yu et al. (2012) combined SEM and XRD analysis of a sandstone sample pre- and post-CO₂ injection and found that minerals such as K-feldspar, albite, calcite and ankerite were variably dissolved and a small amount of kaolinite was generated after the experiments. Wang et al. (2016) found that minerals such as smectite, biotite and kaolinite dissolved to some extent, whereas quartz, plagioclase, illite and chlorite precipitated considerably after CO₂ injection. Figure 5 shows the mineralogical change before and after ScCO₂ injection obtained by XRD analysis in this study. Based on the figure, it can be inferred that the interactions involve reactive mineral dissolution (e.g., calcite) and cause a reduction of acidity (Eq. 2):



The dissolution of minerals can extend to silicates, and the following reactions (Eqs. 3, 4 and 5) may occur (Hiscock 2009; Jin et al. 2016; Ghafoori et al. 2017):

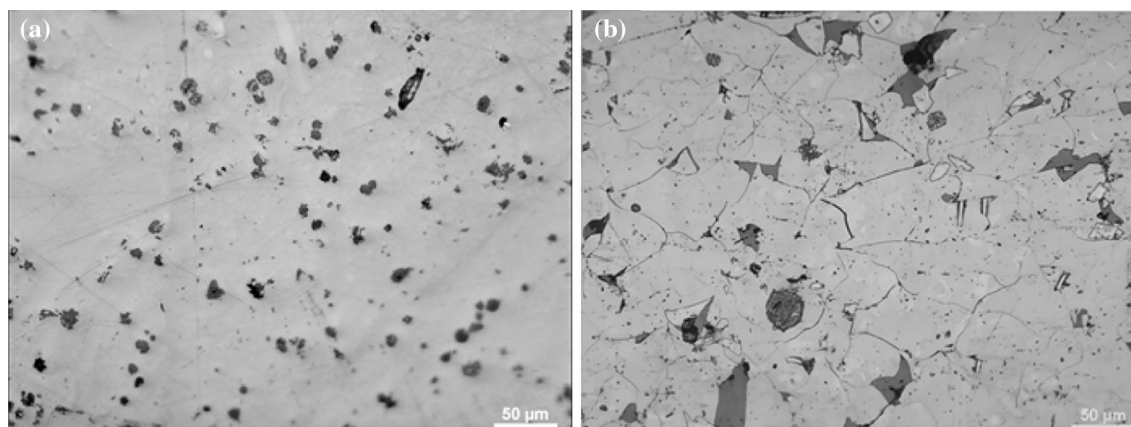
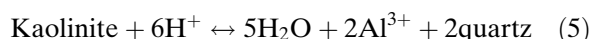
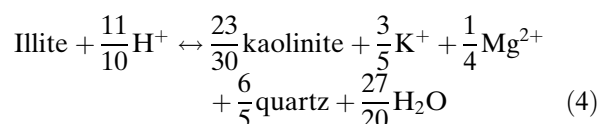
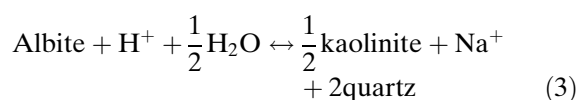


Figure 6. Coal surface feature change obtained by optical microscopy: (a) initial sample; (b) treated sample. Bright color = coal macerals. Dark color = minerals.



As Figure 5 and the chemical equations indicate, kaolinite and quartz are deposited due to the dissolution of albite and illite. While quartz is stable in a weak acid environment, kaolinite can be further dissolved by consuming H^+ and this may cause less kaolinite precipitation than quartz. In addition, it can also be inferred from the reactions that significant precipitation of chlorite ($(\text{Mg,Fe})_3(\text{Si,Al})_4\text{O}_{10}$), feldspar (KAlSi_3O_8) and analcime ($\text{Na}(\text{AlSi}_2\text{O}_6)\cdot\text{H}_2\text{O}$) happened after saturation, and the dissolution of albite, illite and kaolinite can release the ions of Na^+ , K^+ , Mg^{2+} and Al^{3+} , which is necessary for the precipitation of these minerals.

2-D Surface Feature Change

High-resolution 2-D images were acquired from polished thin sections using optical microscopy. Representative images were chosen for both initial and treated samples with a resolution of $0.18 \mu\text{m}$ per pixel and a field of view of about $230 \times 173 \mu\text{m}$ per image (Fig. 6). As can be seen from the figure, many

cracks were formed after ScCO_2 -water treatment. The 2-D quantitative micro-crack analysis was conducted using a new computational approach (Arená et al. 2014). Each crack was isolated and characterized in terms of geometrical characteristics, including crack length, width and aspect ratio (width/length) (Fig. 7). The statistical distributions of the crack length and width were obtained by fitting lognormal and Gaussian functions, respectively. The orientation in the 2-D images ranged from 0° to 360° , where 0° was a crack parallel to horizontal axis, and the angles were counted as positive in the anticlockwise rotation.

According to Figure 7, 240 cracks were identified in the image and the crack density in the image was approximately 5%. The crack length was in the range of $2.7\text{--}75.3 \mu\text{m}$ with an average value of $11.4 \mu\text{m}$. The crack width was in the range of $0.34\text{--}2 \mu\text{m}$ and the average width was $0.89 \mu\text{m}$. The majority of cracks were oriented between -30° and 30° .

Coal surface feature change was also observed by SEM and the typical surface features before and after ScCO_2 treatment are shown in Figure 8. Compared with the initial sample, significant changes were generated after treatment. First, many cracks were found in the image after treatment, which is consistent with the result obtained by optical microscopy. Coal is a highly heterogeneous rock consisting of a variety of organic matter (macerals such as vitrinite, inertinite and liptinite) mixed with various inorganic minerals, which all differ in adsorbability, swellability and stiffness, and distinct

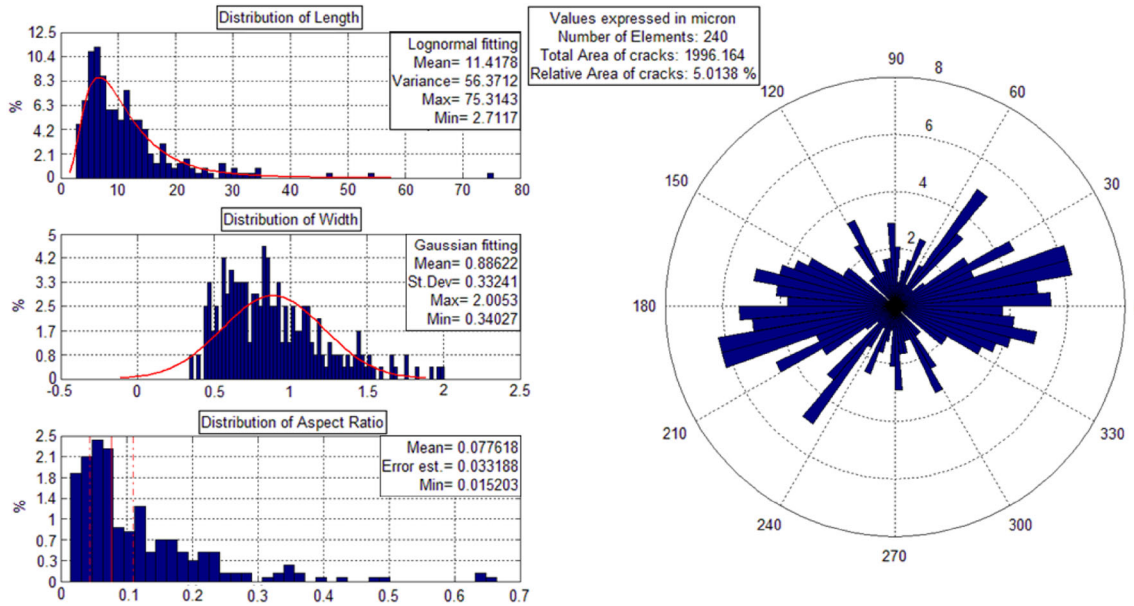


Figure 7. Crack statistics from optical image analysis.

responses of different lithotypes occur with swelling (Karacan and Mitchell 2003; Karacan 2007). Generally, macerals have higher CO₂ adsorption capacities and swelling rates than minerals (Karacan 2007) and even within a given maceral class, differences in swellability are observed (Romanov 2007). Brenner (1983) found that the cracking nature of coal swelling after interacting with solvent is caused primarily by mechanical stresses from uneven swelling rather than by chemical reactions of the solvent with coal. Accordingly, the difference in deformation between the different lithotypes is the main cause of micro-cracking. In Figure 8b, we observed that the micro-cracks were mainly created along the boundaries between gel-like structures (light gray) and the dark gray structures what we infer to be different maceral types. This indicates that un-coordinated deformation and stress concentration localized along the phase boundaries. Elemental analysis by SEM with energy-dispersive X-ray analysis (SEM-EDX) showed that the gel-like structure was organic matter composed of high content of carbon (C), oxygen (O) and small amount of organic sulfur (Fig. 9). The presence of the gel-like structure indicates a coal structural change caused by coal swelling, confirming that the coal underwent physical structure rearrangement. One possible explanation for this phenomenon is that the swelling is more pronounced in the vitrinite group than in other maceral groups

(inertinite and liptinite) present in coal (Karacan 2007) and the gel-like structure is probably formed after vitrinite swelling and relaxing to form a new rubbery structure.

The CO₂ adsorption process not only modifies the physical structure of coal matrix, but also extracts some organic compounds and mobilizes them through the coal seam. Coal's structure is a 3-D cross-linked macromolecular network with free hydrocarbons occluded within the network (Radke et al. 1990; Romanov 2007; Kolak and Burruss 2014). ScCO₂ is a good solvent for hydrocarbon molecules such as benzene, toluene, ethylbenzene, xylenes, and polycyclic aromatic hydrocarbons (PAHs) (Anitescu and Tavlarides 2006; Kolak and Burruss 2006; Wang et al. 2016). In the present study, the hydrocarbon extraction effect is confirmed by the presence of wormholes induced in macerals following ScCO₂ treatment (Fig. 8). The formation of wormholes probably occurs in the texture after hydrocarbon mobilization into the saturation fluid.

2-D Internal Structure Change

Figure 10 shows the internal structure change in a representative region of coal obtained from CT images after treatment with ScCO₂-water. It ap-

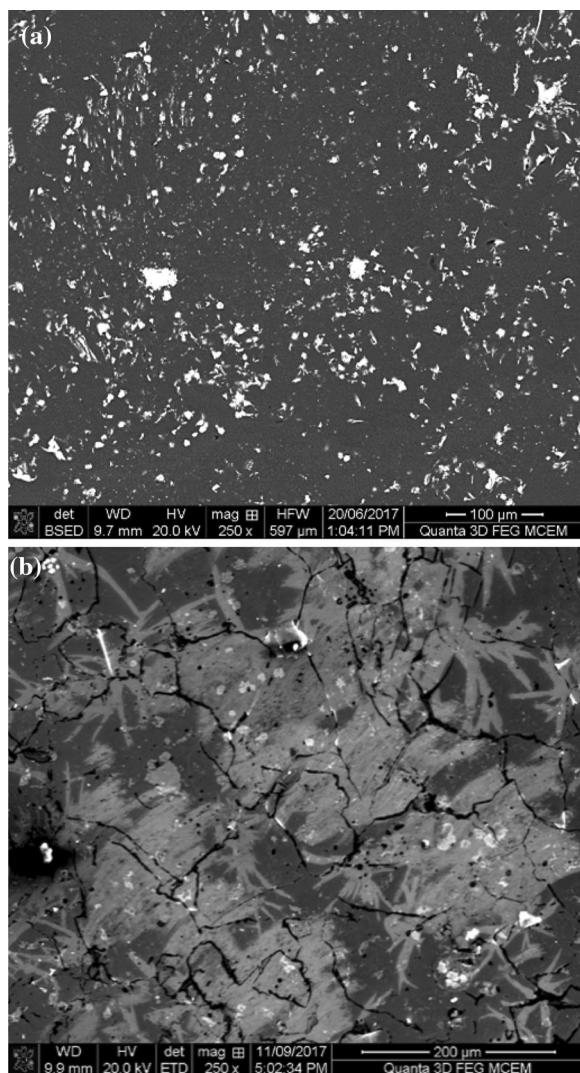


Figure 8. Coal surface feature change obtained by SEM: (a) initial sample (white = mineral and gray = maceral); (b) treated sample (white = mineral, gray = maceral and black = wormholes and fractures).

pears that some minerals are dissolved by the carbonic acid formed during CO_2 dissolution in the water and some macerals are mobilized by ScCO_2 as a good solvent, leading to the emergence of secondary porosity. The carbonic acid and ScCO_2 propagate through the fractures and leach out both minerals and macerals from coal. These changes increase the aperture and length of the existing fracture and therefore porosity and permeability. Field and experimental studies have shown that mineral dissolution also occurs during CO_2 injection in conventional reservoirs, such as sandstone and carbonate, which increases porosity and permeabil-

ity in the near-well region (Gunter et al. 1997; Grigg and Svec 2003; Izgec et al. 2006; Grigg and Svec 2008). Some minerals such as calcite may dissolve readily, which causes an increase in porosity and permeability along the flow channel. Accordingly, a higher flow rate increases the dissolution and forms wormholes. Izgec et al. (2006) observed that CO_2 -water-rock interactions cause small changes in rock porosity with significant change in permeability because of the presence of wormholes.

Figure 11 shows axial images of coal before and after ScCO_2 -water treatment. As can be seen from the figure, many new cracks formed and existing cracks opened after saturation, which accordingly increased the porosity. As the new cracks developed roughly along the maceral-mineral interface, we infer that the micro-cracking was caused by differential swelling, as stated previously. In addition to differential swelling, Yang et al. (2018) found that fracture toughness of coal declined due to the effect of ScCO_2 , which may trigger the initiation of cracks and the propagation of existing cracks. This is because CO_2 adsorption may reduce the surface energy of cracks and lower the crack initiation stress threshold (Viete and Ranjith 2006). Note that free swelling of the unconstrained coal sample in this experiment caused the opening of existing cracks during the coal swelling process. Although the swelling was reversible and cracks shrank back after removing the sample from the reaction chamber, the aperture could not return to the initial stage. The residual crack aperture increase resulted in the existing cracks opening (Fig. 11).

Some authors have also concluded that micro-crack initiation and propagation occur as a result of adsorption-induced differential swelling of coal macerals or drying and shrinkage of coal under unconstrained conditions (Gathitu et al. 2009; Hol et al. 2012). A recent study conducted micro-CT scanning of a coal sample under unconfined stress for three different conditions: as-received, CO_2 pressurized and depressurized (Pirzada et al. 2018). The results showed that CO_2 adsorption closed some preexisting cracks and at the same time caused the formation of new cracks under unconfined stress. In addition, the release of CO_2 caused both preexisting cracks and newly formed cracks to open. The results confirmed that the new cracks were formed in the CO_2 adsorption process rather than the CO_2 desorption process and CO_2 desorption only reopened the preexisting cracks and new cracks. However, the influence of ScCO_2 on the cracking behavior of coals

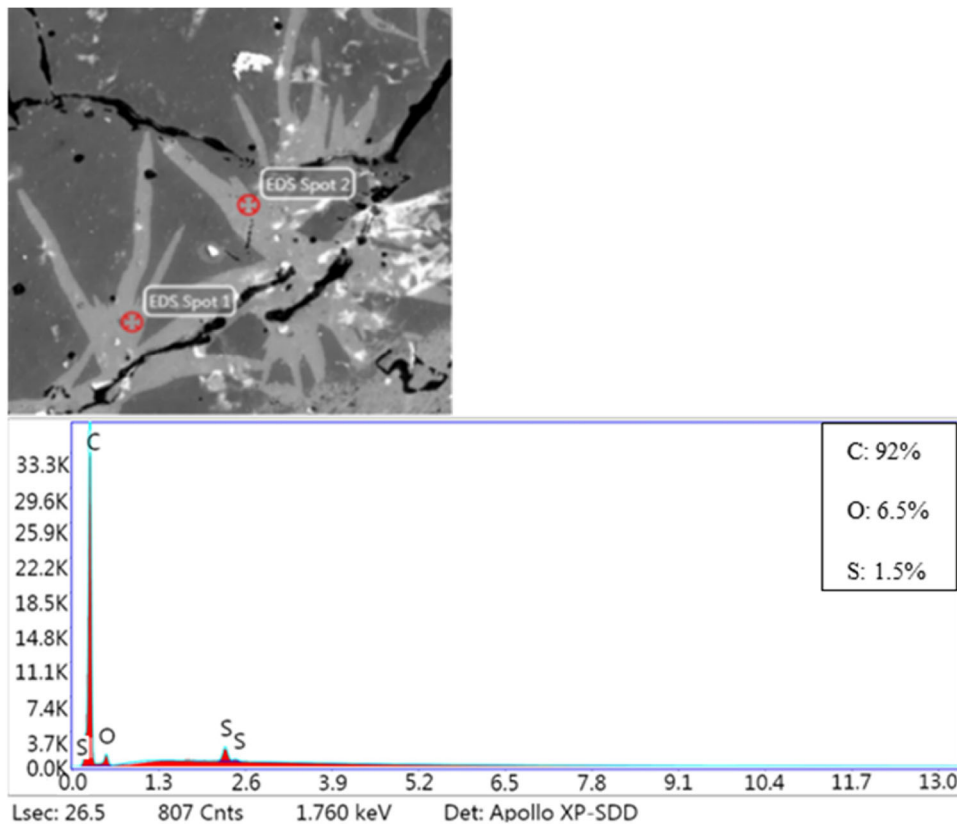


Figure 9. SEM images with elemental analysis (wt% measured by EDS).

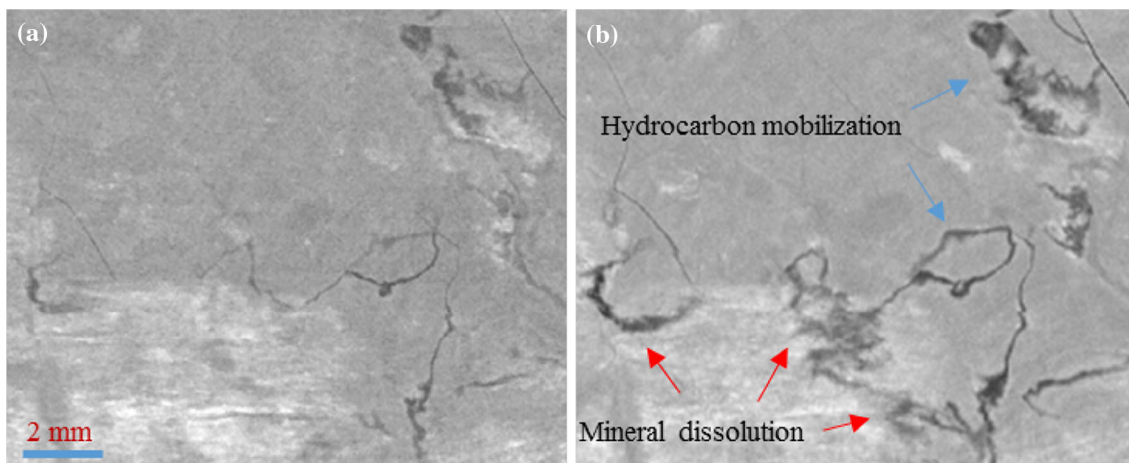


Figure 10. Coal internal structure change obtained by CT images: (a) initial sample; (b) treated sample. Bright color = minerals. Gray color = macerals. Black color = voids.

is also affected by in situ stresses. For example, Zhang and his colleagues conducted a series of micro-CT scanning experiments under in situ stress

conditions to investigate the changes in coal and limestone micro-structures due to ScCO₂ and water saturation (Zhang et al. 2016a, b, c; Lebedev et al.

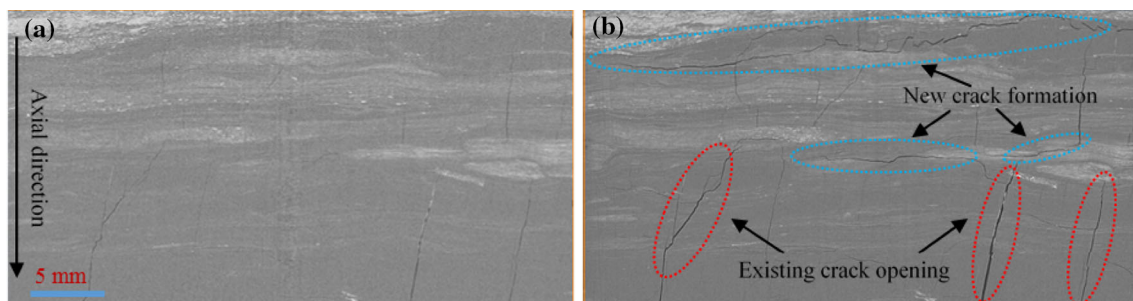


Figure 11. Coal internal structure change in axial CT images: (a) initial sample; (b) treated sample. Bright color = minerals. Gray color = macerals. Black color = voids.

Table 3. Summary of mechanisms and resultant changes in coal

Cause		Resultant change		
Type	Mechanism	Maceral fraction	Mineral fraction	Fracture fraction
Physical	Stress-induced fracturing	None	None	Increase
	Fracture opening	None	None	Increase
Chemical	Mineral dissolution	None	Decrease	Increase
	Hydrocarbon mobilization	Decrease	None	Increase

Fracture fraction corresponds to void spaces including both connected and isolated porosity larger than image resolution of 17.8 microns

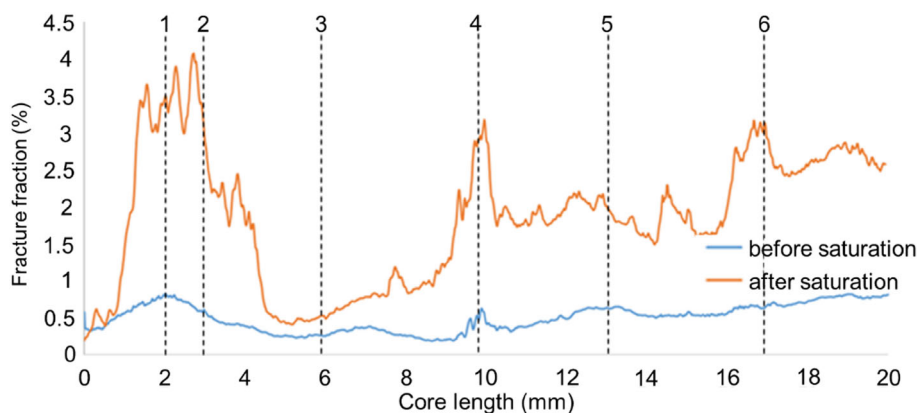
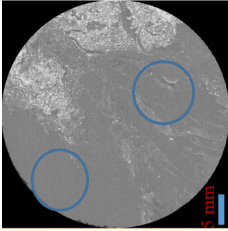
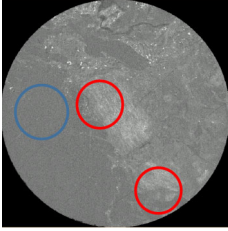
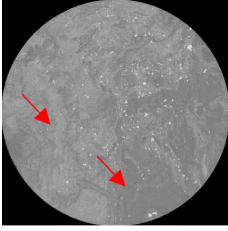
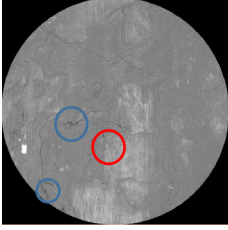
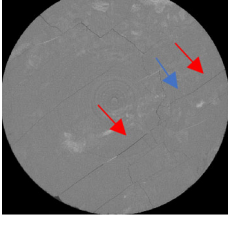
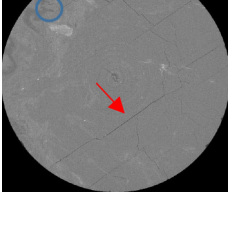
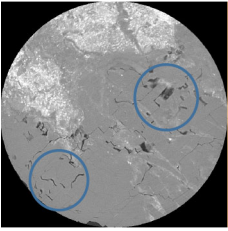
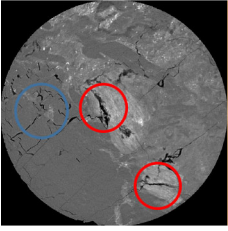
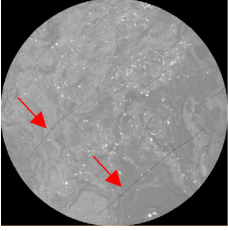
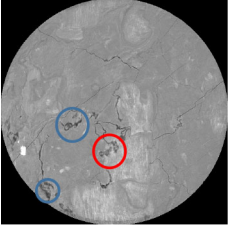
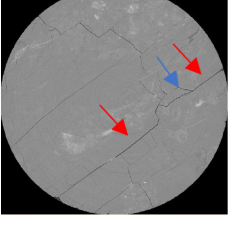
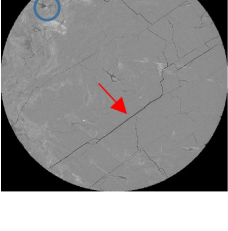


Figure 12. Changes in fracture fraction for each slice along sample length.

2017; Zhang et al. 2018a, b). They showed that CO₂ adsorption-induced swelling closed the existing cracks in coal and caused a significant permeability reduction under confined stress; however, some new cracks were formed in minerals due to internal swelling stress (Zhang et al. 2016b). This indicates that crack behavior is complex under in situ stress conditions but swelling-induced crack closure may

dominate during CO₂ adsorption. The significant crack formation and opening phenomena under free swelling conditions in our study may not occur under confined stress. However, we also observed secondary porosity induced by mineral dissolution and the hydrocarbon mobilization effect, which may still occur under in situ stress conditions. The changes in coal structure and permeability under in situ stress

Table 4. Micro-structural change and dominant mechanisms in selected locations

Location	1	2	3	4	5	6
Before treatment						
After treatment						
Distance from top end (mm)	2	3	6	10	13	17
Dominant change	Hydrocarbon mobilization (blue circles)	Hydrocarbon mobilization (blue circle) and mineral dissolution (red circles)	Swelling-induced existing fracture opening (red arrows)	Hydrocarbon mobilization (blue circles) and mineral dissolution (red circle)	Swelling-induced existing fracture opening (red arrows) and new fracture formation (blue arrow)	Hydrocarbon mobilization (blue circles) and swelling-induced existing fracture opening (red arrow)

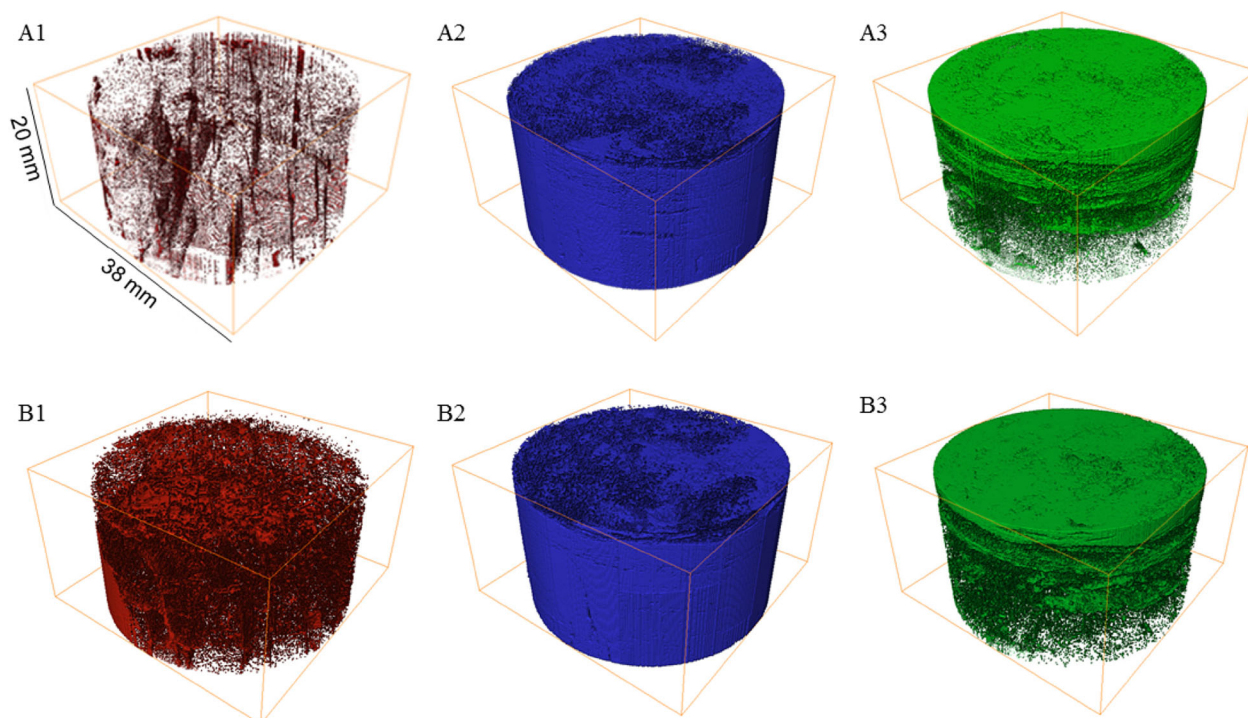


Figure 13. 3-D visualizations of different phases before and after ScCO₂ treatment: (A) initial sample; (B) treated sample (1 = fractures and pores, 2 = macerals, and 3 = minerals).

Table 5. Volume fractions of different phases before and after ScCO₂-water treatment

Phase	Volume fraction	
	Initial sample (%)	Treated sample (%)
Pore/crack	0.63	2.22
Maceral	85.48	84.19
Mineral	13.90	13.60

conditions are complex, because the changes result from the combined effect of swelling, mineral dissolution and hydrocarbon mobilization. A further micro-CT investigation under in situ stress conditions will be conducted in the future, and the results will be compared with those reported in the present study.

Overall, the changes under unconfined stress shown in this study, including mineral dissolution, hydrocarbon mobilization, stress-induced fracturing and fracture opening, finally enhance coal porosity. These mechanisms and the resultant micro-structural changes in coal are summarized in Table 3.

Figure 12 shows the fracture fraction (porosity) change of the sample for each slice along the entire length of the core. As the figure shows, although an increase in porosity was obtained along the length of the whole sample, the extent of porosity increase was dependent on the location in the sample. This is because a different mechanism may dominate in a specific location due to the highly heterogeneous nature of coal. Six typical locations were selected from Figure 12 and Table 4 shows the corresponding micro-structural changes and the dominant mechanisms. It can be inferred that mineral dissolution and hydrocarbon mobilization significantly increase porosity compared with swelling-induced new fractures and fracture opening.

3-D Micro-Structural Change

3-D representations of the segmented phases of samples before and after ScCO₂-water treatment are presented in Figure 13, and the volume fractions of each component measured are shown in Table 5. It should be noted that the mineral matter content (13.90%) of the initial sample is similar to the ash

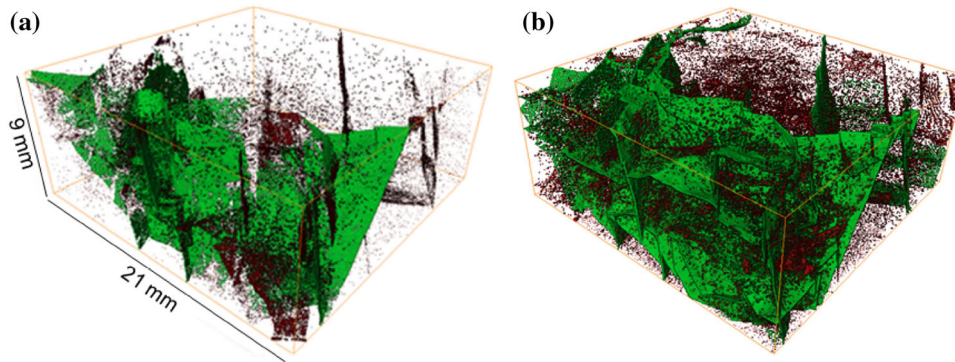


Figure 14. Pore networks of sample before and after ScCO₂ treatment: (a) initial sample; (b) treated sample. Green = connected porosity. Red = non-connected porosity.

Table 6. Results of porosity and permeability change due to ScCO₂ treatment

	Initial sample	Treated sample	Change
Total porosity	0.53%	2.7%	+ 4.1 times
Connected porosity	0.35%	2.05%	+ 4.9 times
Permeability	40.6 mD	1190.4 mD	+ 28.3 times

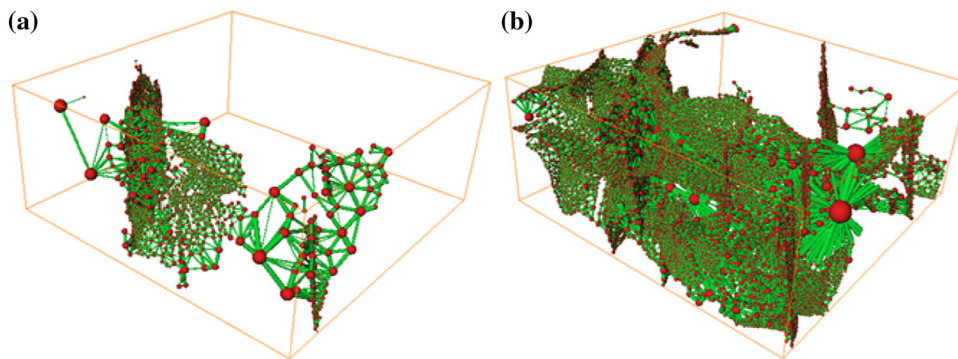


Figure 15. Pore network models of connected pore network: (a) initial sample; (b) treated sample.

content (13.16%), and the coal maceral content (85.48%) of the initial sample is roughly the same as the volatile matter and fixed carbon components (85.53%) determined by proximate analysis. This comparison verifies the accuracy of the segmentation results.

According to the results, the porosity of coal increased from 0.63 to 2.22%. Macerals are the main component in coal and these decreased by 1.29%, whereas minerals decreased by 0.3%. These changes are consistent with those observed in the 2-D ima-

ges, and result from mineral dissolution and hydrocarbon mobilization, as stated previously.

Connectivity and Permeability

To further analyze the connectivity and permeability of the pore networks before and after treatment, we extracted two sub-volumes (regions of interest) from the same position in the pore networks before and after treatment to reduce the

Table 7. Pore and throat attributes of PNMs before and after treatment

Sample	Pore attributes							Throat attributes							
	Total no.	Min. (μm)	Max. (μm)	Avg. (μm)	Volume (mm^3)	Area (mm^2)	Coordination no.	Avg. coordination no.	Total no.	Min. (μm)	Max. (μm)	Avg. (μm)	Area (mm^2)	Channel length (μm)	Avg. channel length (μm)
Initial	4593	17.0	404.9	70.9	12.8	782.1	1–35	6	12,895	17.0	182.0	39.1	73.5	32.4–4579	231.2
Treated	24,010	17.6	675.1	76.0	83.4	4203.3	1–94	6	69,309	17.0	308.3	41.8	479.5	19.3–3689	252.0

computational burden (Fig. 14). The shape of a sample is usually irregular, and a regular region of interest is therefore convenient for further pore structure characterization and flow simulation. Connectivity analysis was then conducted on the sub-volumes, and the connected porosity was displayed in green and non-connected porosity was displayed in red. The resultant porosity and permeability changes due to ScCO_2 treatment are shown in Table 6. After treatment, the total porosity and connected porosity increased by 4.1 and 4.9 times, respectively. Some isolated porosities became interconnected and some new fractures were generated after saturation. As a result, the permeability calculated using the lattice Boltzmann method increased by 28 times after treatment. Because permeability varies with the square of the fracture aperture, permeability increases significantly as larger fractures are encountered.

Pore Network Model

Connected pore and fracture (throat) properties (e.g., pore radius, volume, connectivity and fracture length) determine pore porosity and permeability. To further characterize the pore structure alteration due to ScCO_2 -water treatment, PNMs were extracted from the connected pore spaces before and after treatment. In PNMs, pores are connected by the throats to represent real pore spaces. As Figure 15 and Table 7 show, significantly more pores and throats were generated after ScCO_2 -water treatment, which is consistent with the porosity increase mentioned above.

PNMs can also provide insights into pore and throat size distribution and pore network connectivity. Figure 16 reveals the connected pore radius, area and volume distributions for initial and treated samples. The pore size distribution shows pores with equivalent radii at 50–100 μm were dominant in both samples, and the pores with equivalent radii below 150 μm contributed 96% and 98% of the total pore numbers in initial and treated samples, which indicate that most of the pores in the coal samples were smaller than 150 μm in radius. After treatment, many pores were formed increasing from 4593 to 24,010 and the average pore radius also increased from 70.9 to 76.0 μm (Table 7).

Figure 17 shows both cumulative pore volume and area vs. pore size display a logistic function relationship, which indicates the pores with sizes of

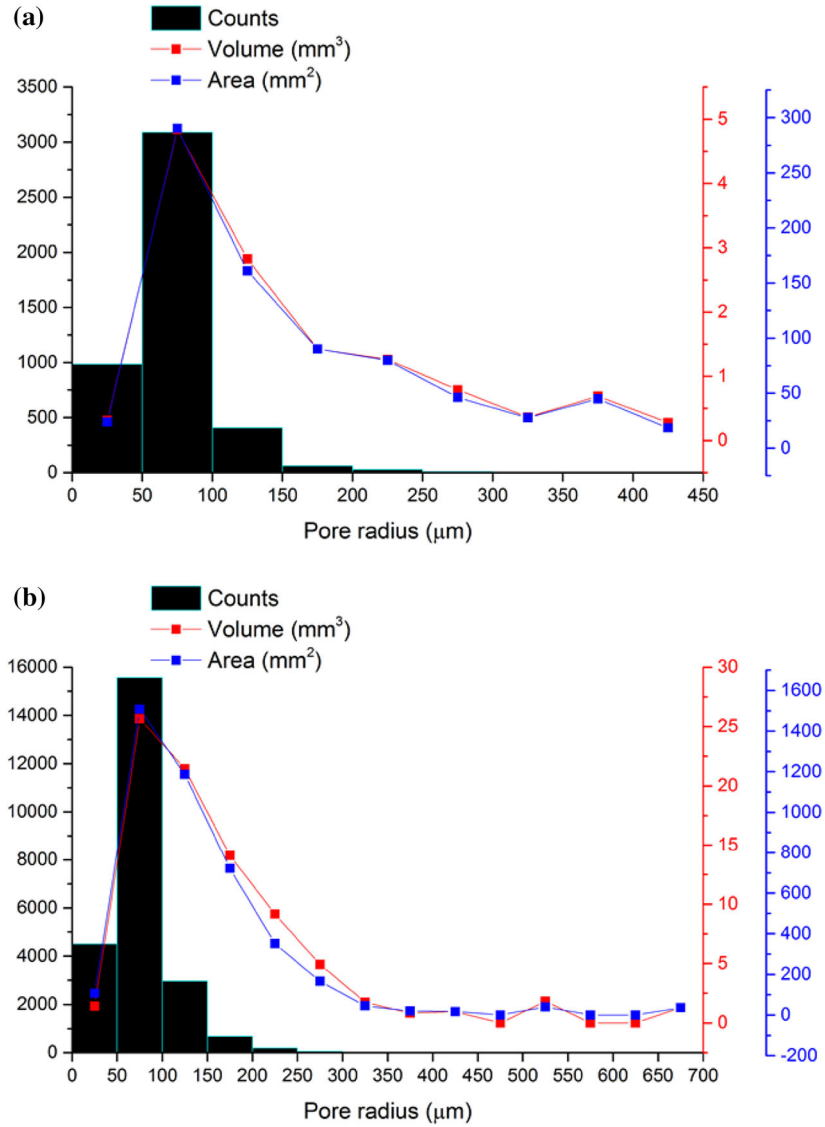


Figure 16. Pore size, area and volume distribution: (a) initial sample; (b) treated sample.

50–300 μm make the main contribution to pore volume and area. In addition, the gradient of the curve in treated samples is much higher than that of the initial samples, which indicates more pores pre-

dominated between 50 and 300 μm in treated samples.

The coordination number, defined as the number of neighbors connected to a given pore, reflects the connectivity of pores. As Figure 17 indicates, the

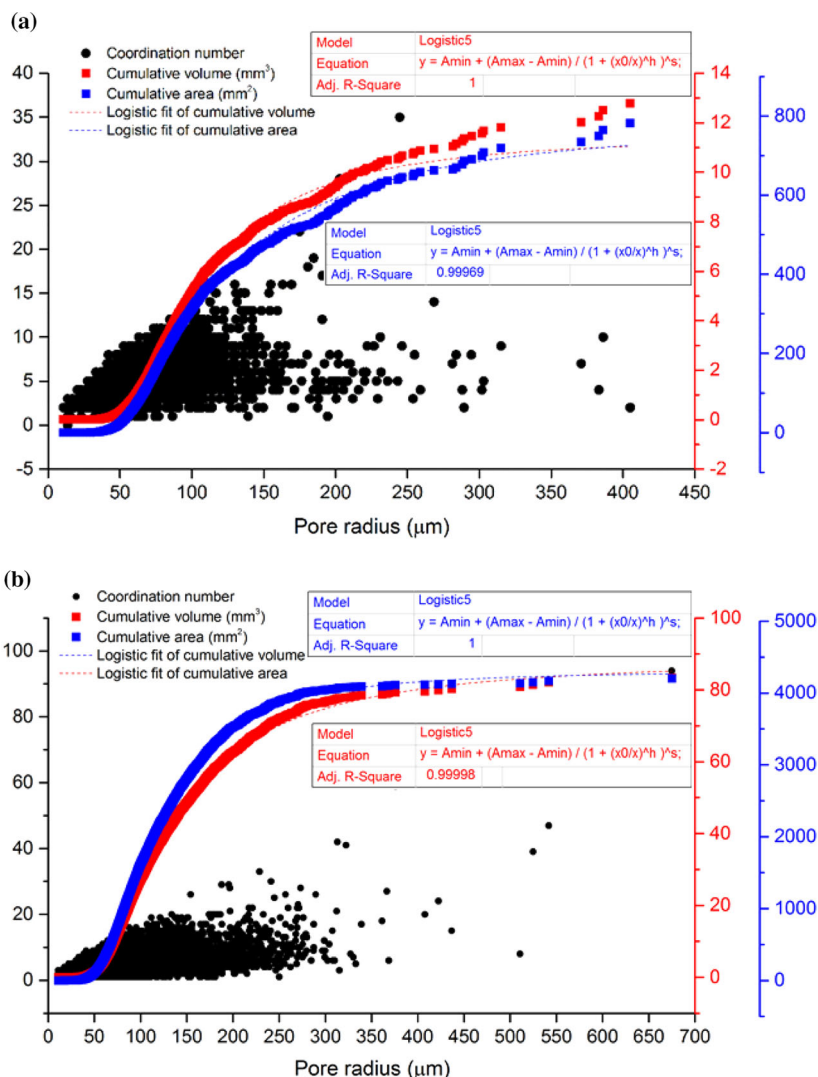


Figure 17. Coordination number, cumulative area and volume vs. pore radius: (a) initial sample; (b) treated sample.

coordination number may vary in the same pore size, but larger pores generally have high coordination numbers. The coordination number distribution exhibited a Gaussian distribution (Fig. 18), and significantly more pores were developed for all coordination number levels in treated samples. In addition, after treatment, pores with high coordina-

tion (> 10) emerged, which were not well-developed before treatment. Therefore, many well-connected pores developed in the treated samples, resulting in high connectivity and permeability, as stated above.

Statistical analysis of the throat attributes was also conducted. Similar to the pore radius distribution, the throat radius distribution followed a

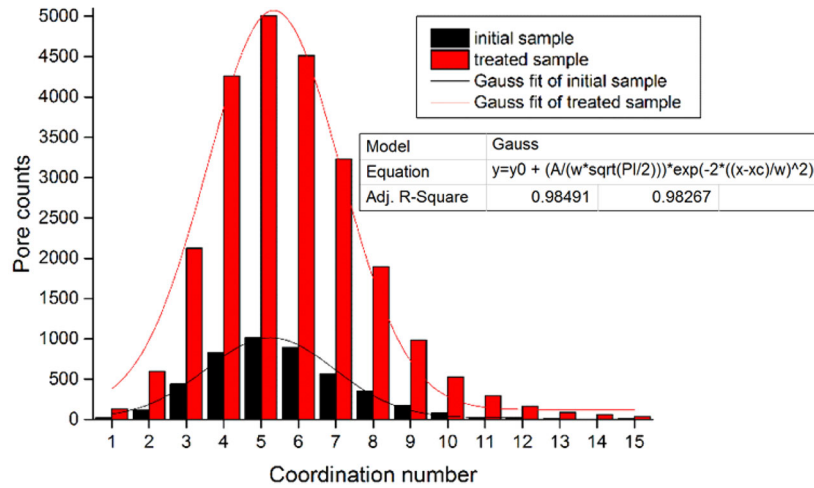


Figure 18. Coordination number distribution.

Gaussian function and cumulative pore area followed a logistic function (Figs. 19a and 20). As for the throat length, the distribution followed a log-normal function, and although the throat lengths had a wide range (Fig. 19b and Table 7), shorter throats with lengths less than 500 μm accounted for 94% and 91% of the total number of throats in initial and treated samples, respectively. After treatment, a large number of throats were generated, resulting in a significant increase of throat area (Fig. 20 and Table 7). The average throat radius and length increased from 39.1 to 41.8 μm and from 231.2 to 252.0 μm, respectively (Table 7).

CONCLUSIONS

The exposure to ScCO₂-water results in significant changes in the physical and chemical structures of coal. The modifications are associated

with mineral dissolution, hydrocarbon mobilization and swelling-induced fracturing and crack opening. ScCO₂-water-coal interaction generated many wormholes and cracks in coal, which were observed by optical microscopy, SEM and micro-CT images. The porosity and permeability of the coal sample were significantly enhanced by ScCO₂-water treatment, which was quantified by micro-CT scanning. Such interactions promoted the pore/throat size and more isolated pores became accessible after saturation, improving the pore network connectivity and making the pore space more accessible. This represents a positive phenomenon for ECBM production, as the introduction of CO₂ may result in increased porosity and improved permeability. However, these comparisons and conclusions were drawn from tests done in an unconfined chamber and with unstressed samples, and the influence of ScCO₂-water on coal’s micro-structure is also affected by in situ stresses. The changes of coal

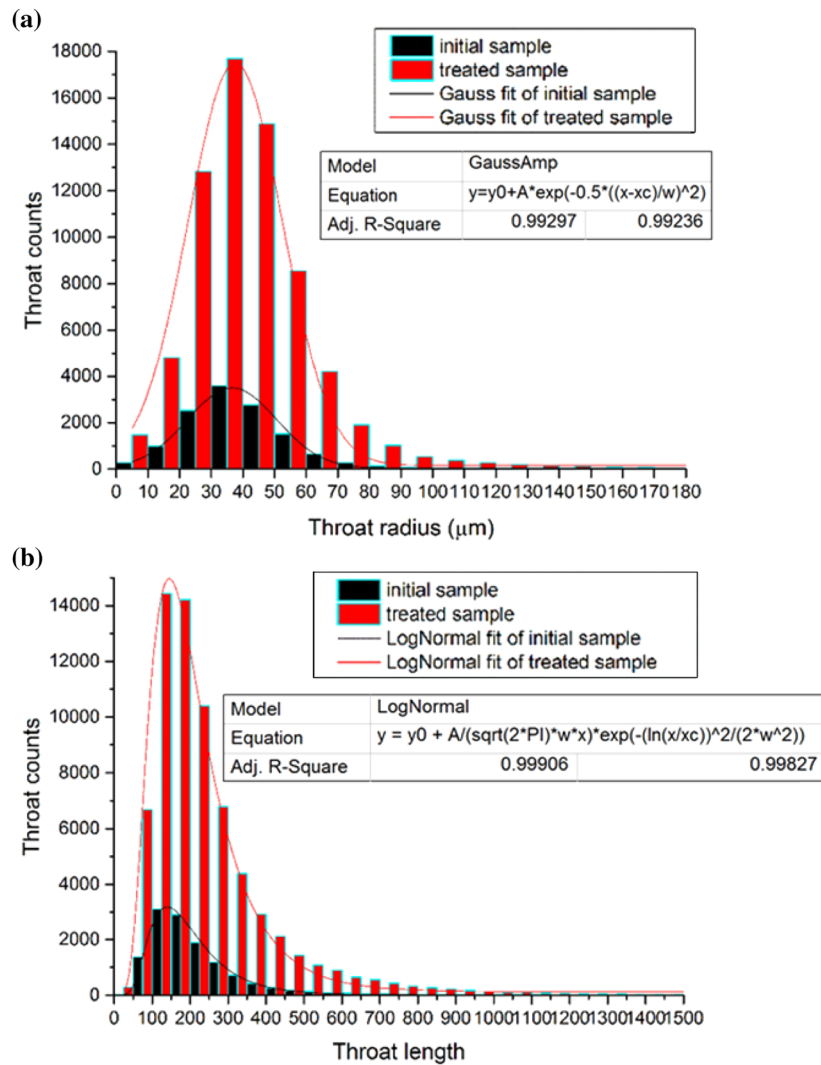


Figure 19. Throat attributes: (a) throat radius distribution; (b) throat length distribution.

structure and permeability under in situ stress conditions are complex and a micro-CT investiga-

tion under in situ stress conditions will be conducted in future.

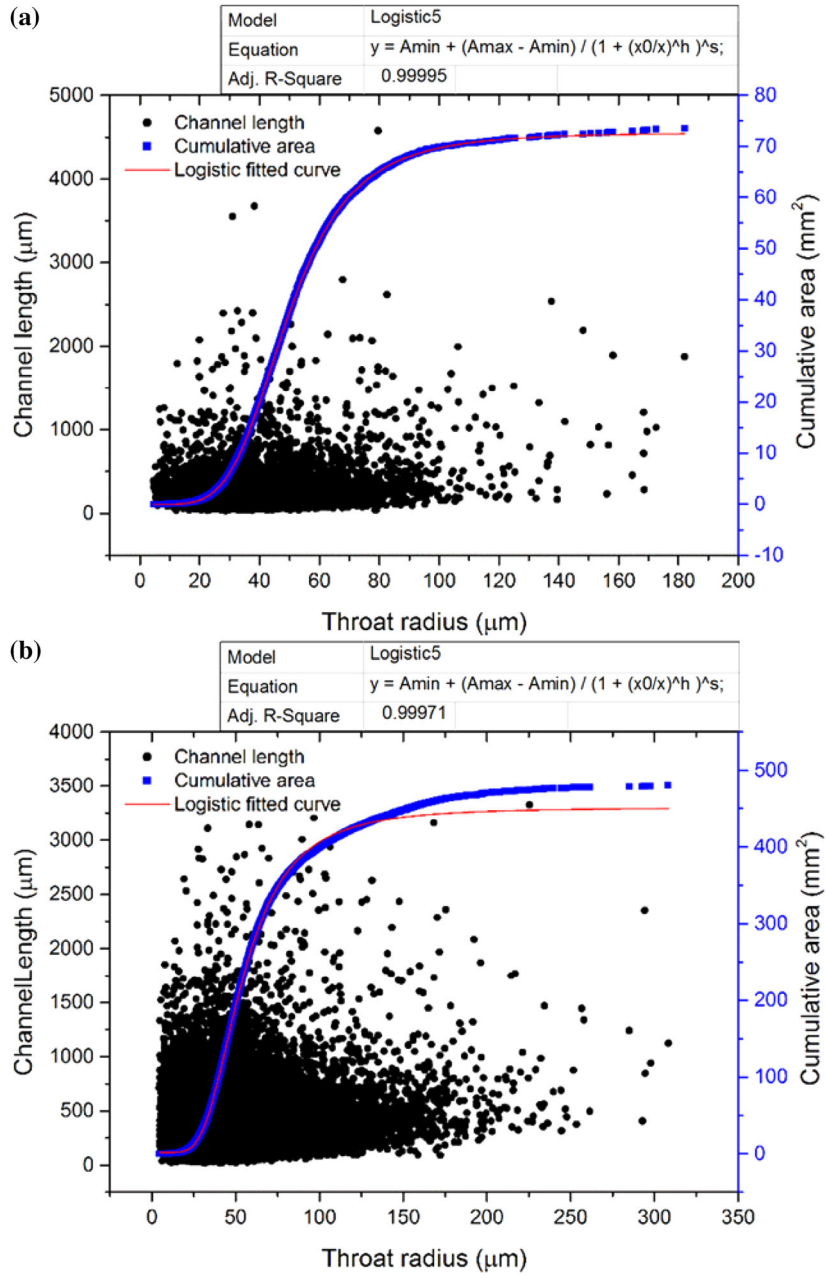


Figure 20. Channel length and cumulative throat area vs. throat radius: **(a)** initial sample; **(b)** treated sample.

ACKNOWLEDGMENTS

The CT scanning was undertaken on the Imaging and Medical beamline at the Australian Synchrotron, and we record our great appreciation of Dr. Anton Maksimenko and Dr. Chris Hall for their assistance in recording the CT images.

REFERENCES

- Anderson, S. T. (2017a). Cost implications of uncertainty in CO₂ storage resource estimates: A review. *Natural Resources Research*, 26(2), 137–159.
- Anderson, S. T. (2017b). Risk, liability, and economic issues with long-term CO₂ storage—A review. *Natural Resources Research*, 26(1), 89–112.
- Andrew, M., Bijeljic, B., & Blunt, M. J. (2013). Pore-scale imaging of geological carbon dioxide storage under in situ conditions. *Geophysical Research Letters*, 40(15), 3915–3918.
- Anitescu, G., & Tavlirides, L. (2006). Supercritical extraction of contaminants from soils and sediments. *The Journal of Supercritical Fluids*, 38(2), 167–180.
- Apps, J., Zheng, L., Zhang, Y., Xu, T., & Birkholzer, J. (2010). Evaluation of potential changes in groundwater quality in response to CO₂ leakage from deep geologic storage. *Transport in Porous Media*, 82(1), 215–246.
- Arena, A., Delle Piane, C., & Sarout, J. (2014). A new computational approach to cracks quantification from 2D image analysis: Application to micro-cracks description in rocks. *Computers & Geosciences*, 66, 106–120.
- Blunt, M. J. (2001). Flow in porous media—Pore-network models and multiphase flow. *Current Opinion in Colloid & Interface Science*, 6(3), 197–207.
- Brenner, D. (1983). In situ microscopic studies of the solvent-swelling of polished surfaces of coal. *Fuel*, 62(11), 1347–1350. [https://doi.org/10.1016/S0016-2361\(83\)80022-2](https://doi.org/10.1016/S0016-2361(83)80022-2).
- Day, S., Fry, R., & Sakurovs, R. (2008). Swelling of Australian coals in supercritical CO₂. *International Journal of Coal Geology*, 74(1), 41–52.
- De Boever, E., Varloteaux, C., Nader, F. H., Foubert, A., Békri, S., Youssef, S., et al. (2012). Quantification and prediction of the 3D pore network evolution in carbonate reservoir rocks. *Oil & Gas Science and Technology-Revue d'IFP Energies nouvelles*, 67(1), 161–178.
- Dong, H., Fjeldstad, S., Alberts, L., Roth, S., Bakke, S., & Øren, P.-E. (2008). Pore network modelling on carbonate: A comparative study of different micro-CT Network extraction methods. In *International symposium of the society of core analysts, Society of Core Analysts, 2008*.
- Dong, B., Meng, M., Qiu, Z., Lu, Z., Zhang, Y., & Zhong, H. (2019). Formation damage prevention using microemulsion in tight sandstone gas reservoir. *Journal of Petroleum Science and Engineering*, 173, 101–111. <https://doi.org/10.1016/j.petrol.2018.10.003>.
- Farquhar, S., Pearce, J., Dawson, G., Golab, A., Sommacal, S., Kirste, D., et al. (2015). A fresh approach to investigating CO₂ storage: Experimental CO₂–water–rock interactions in a low-salinity reservoir system. *Chemical Geology*, 399, 98–122.
- Fujioka, M., Yamaguchi, S., & Nako, M. (2010). CO₂-ECBM field tests in the Ishikari Coal Basin of Japan. *International Journal of Coal Geology*, 82(3), 287–298. <https://doi.org/10.1016/j.coal.2010.01.004>.
- Gathitu, B. B., Chen, W.-Y., & McClure, M. (2009). Effects of coal interaction with supercritical CO₂: Physical structure. *Industrial and Engineering Chemistry Research*, 48(10), 5024–5034.
- Ghafoori, M., Tabatabaei-Nejad, S. A., & Khodapanah, E. (2017). Modeling rock-fluid interactions due to CO₂ injection into sandstone and carbonate aquifer considering salt precipitation and chemical reactions. *Journal of Natural Gas Science and Engineering*, 37, 523–538.
- Grigg, R., & Svec, R. (2003). Co-injected CO₂-brine interactions with Indiana Limestone. In *SCA2003-19, presented at the Society of Core Analysts Convention SCA, 2003*.
- Grigg, R. B., & Svec, R. (2008). Injectivity changes and CO₂ retention for EOR and sequestration projects. In *SPE symposium on improved oil recovery, 2008*. Society of Petroleum Engineers.
- Gunter, W., Wiwehar, B., & Perkins, E. (1997). Aquifer disposal of CO₂-rich greenhouse gases: Extension of the time scale of experiment for CO₂-sequestering reactions by geochemical modelling. *Mineralogy and Petrology*, 59(1–2), 121–140.
- He, X., & Luo, L.-S. (1997). Lattice Boltzmann model for the incompressible Navier–Stokes equation. *Journal of Statistical Physics*, 88(3), 927–944.
- Hiscock, K. M. (2009). *Hydrogeology: Principles and practice*. Hoboken: Wiley.
- Hol, S., Spiers, C. J., & Peach, C. J. (2012). Microfracturing of coal due to interaction with CO₂ under unconfined conditions. *Fuel*, 97, 569–584.
- Izgec, O., Demiral, B., Bertin, H. J., & Akin, S. (2006). Experimental and numerical modelling of direct injection of CO₂ into carbonate formations. In *SPE annual technical conference and exhibition, 2006*. Society of Petroleum Engineers.
- Jin, M., Ribeiro, A., Mackay, E., Guimarães, L., & Bagudu, U. (2016). Geochemical modelling of formation damage risk during CO₂ injection in saline aquifers. *Journal of Natural Gas Science and Engineering*, 35, 703–719.
- Karacan, C. Ö. (2007). Swelling-induced volumetric strains internal to a stressed coal associated with CO₂ sorption. *International Journal of Coal Geology*, 72(3), 209–220. <https://doi.org/10.1016/j.coal.2007.01.003>.
- Karacan, C. Ö., & Mitchell, G. D. (2003). Behavior and effect of different coal microlithotypes during gas transport for carbon dioxide sequestration into coal seams. *International Journal of Coal Geology*, 53(4), 201–217.
- Kolak, J. J., & Burruss, R. C. (2006). Geochemical investigation of the potential for mobilizing non-methane hydrocarbons during carbon dioxide storage in deep coal beds. *Energy & Fuels*, 20(2), 566–574.
- Kolak, J. J., & Burruss, R. C. (2014). The use of solvent extractions and solubility theory to discern hydrocarbon associations in coal, with application to the coal–supercritical CO₂ system. *Organic Geochemistry*, 73, 56–69. <https://doi.org/10.1016/j.orggeochem.2014.05.002>.
- Kutchko, B. G., Goodman, A. L., Rosenbaum, E., Natesakhawat, S., & Wagner, K. (2013). Characterization of coal before and after supercritical CO₂ exposure via feature relocation using field-emission scanning electron microscopy. *Fuel*, 107, 777–786.
- Larsen, J. W. (2004). The effects of dissolved CO₂ on coal structure and properties. *International Journal of Coal Geology*, 57(1), 63–70.
- Lebedev, M., Zhang, Y., Sarmadivaleh, M., Barifcani, A., Al-Khdeewi, E., & Iglauer, S. (2017). Carbon geosequestration in limestone: Pore-scale dissolution and geomechanical weakening. *International Journal of Greenhouse Gas Control*, 66, 106–119.
- Li, W., Liu, H., & Song, X. (2017). Influence of fluid exposure on surface chemistry and pore-fracture morphology of various rank coals: Implications for methane recovery and CO₂ storage. *Energy & Fuels*, 31(11), 12552–12569.

- Liu, S., Busch, A., Ma, J., Sang, S., Wang, T., Du, Y., et al. (2018). The effects of supercritical CO₂ on mesopore and macropore structure in bituminous and anthracite coal. *Fuel*, 223, 32–43.
- Massarotto, P., Golding, S. D., Bae, J. S., Iyer, R., & Rudolph, V. (2010). Changes in reservoir properties from injection of supercritical CO₂ into coal seams—A laboratory study. *International Journal of Coal Geology*, 82(3), 269–279. <https://doi.org/10.1016/j.coal.2009.11.002>.
- Mathews, J. P., Campbell, Q. P., Xu, H., & Halleck, P. (2017). A review of the application of X-ray computed tomography to the study of coal. *Fuel*, 209, 10–24.
- Mazumder, S., Van Hemert, P., Bruining, J., Wolf, K.-H., & Drabe, K. (2006). In situ CO₂-coal reactions in view of carbon dioxide storage in deep unminable coal seams. *Fuel*, 85(12), 1904–1912.
- Mazumder, S., & Wolf, K. H. (2008). Differential swelling and permeability change of coal in response to CO₂ injection for ECBM. *International Journal of Coal Geology*, 74(2), 123–138. <https://doi.org/10.1016/j.coal.2007.11.001>.
- Meng, M., & Qiu, Z. (2018). Experiment study of mechanical properties and microstructures of bituminous coals influenced by supercritical carbon dioxide. *Fuel*, 219, 223–238. <https://doi.org/10.1016/j.fuel.2018.01.115>.
- Pan, Z., Connell, L. D., & Camilleri, M. (2010). Laboratory characterisation of coal reservoir permeability for primary and enhanced coalbed methane recovery. *International Journal of Coal Geology*, 82(3–4), 252–261.
- Perera, M., Ranjith, P., Airey, D., & Choi, S.-K. (2011a). Sub- and super-critical carbon dioxide flow behavior in naturally fractured black coal: An experimental study. *Fuel*, 90(11), 3390–3397.
- Perera, M. S. A., Ranjith, P. G., & Peter, M. (2011b). Effects of saturation medium and pressure on strength parameters of Latrobe Valley brown coal: Carbon dioxide, water and nitrogen saturations. *Energy*, 36(12), 6941–6947. <https://doi.org/10.1016/j.energy.2011.09.026>.
- Perera, M. S. A., Ranjith, P. G., & Viète, D. R. (2013). Effects of gaseous and super-critical carbon dioxide saturation on the mechanical properties of bituminous coal from the Southern Sydney Basin. *Applied Energy*, 110, 73–81. <https://doi.org/10.1016/j.apenergy.2013.03.069>.
- Pirzada, M. A., Zoorabadi, M., Ramandi, H. L., Canbulat, I., & Roshan, H. (2018). CO₂ sorption induced damage in coals in unconfined and confined stress states: A micrometer to core scale investigation. *International Journal of Coal Geology*, 198, 167–176.
- Radke, M., Willsch, H., & Teichmüller, M. (1990). Generation and distribution of aromatic hydrocarbons in coals of low rank. *Organic Geochemistry*, 15(6), 539–563. [https://doi.org/10.1016/0146-6380\(90\)90101-5](https://doi.org/10.1016/0146-6380(90)90101-5).
- Ranathunga, A. S., Perera, M. S. A., & Ranjith, P. G. (2016a). Influence of CO₂ adsorption on the strength and elastic modulus of low rank Australian coal under confining pressure. *International Journal of Coal Geology*, 167, 148–156. <https://doi.org/10.1016/j.coal.2016.08.027>.
- Ranathunga, A. S., Perera, M. S. A., Ranjith, P. G., & Bui, H. (2016b). Super-critical CO₂ saturation-induced mechanical property alterations in low rank coal: An experimental study. *The Journal of Supercritical Fluids*, 109, 134–140. <https://doi.org/10.1016/j.supflu.2015.11.010>.
- Reucroft, P., & Sethuraman, A. (1987). Effect of pressure on carbon dioxide induced coal swelling. *Energy & Fuels*, 1(1), 72–75.
- Romanov, V. (2007). Coal chemistry for mechanical engineers: From macromolecular thermodynamics to reservoir simulation. *Energy & Fuels*, 21(3), 1646–1654.
- Shan, X., & Chen, H. (1993). Lattice Boltzmann model for simulating flows with multiple phases and components. *Physical Review E*, 47(3), 1815.
- Taylor, H. F., O'Sullivan, C., & Sim, W. W. (2015). A new method to identify void constrictions in micro-CT images of sand. *Computers and Geotechnics*, 69(Supplement C), 279–290. <https://doi.org/10.1016/j.compgeo.2015.05.012>.
- Viète, D. R., & Ranjith, P. G. (2006). The effect of CO₂ on the geomechanical and permeability behaviour of brown coal: Implications for coal seam CO₂ sequestration. *International Journal of Coal Geology*, 66(3), 204–216. <https://doi.org/10.1016/j.coal.2005.09.002>.
- Wang, K., Xu, T., Wang, F., & Tian, H. (2016). Experimental study of CO₂-brine-rock interaction during CO₂ sequestration in deep coal seams. *International Journal of Coal Geology*, 154, 265–274.
- White, C. M., Smith, D. H., Jones, K. L., Goodman, A. L., Jikich, S. A., LaCount, R. B., et al. (2005). Sequestration of carbon dioxide in coal with enhanced coalbed methane recovery: A review. *Energy & Fuels*, 19(3), 659–724.
- Wigand, M., Carey, J., Schütt, H., Spangenberg, E., & Erzinger, J. (2008). Geochemical effects of CO₂ sequestration in sandstones under simulated in situ conditions of deep saline aquifers. *Applied Geochemistry*, 23(9), 2735–2745.
- Yang, J., Lian, H., Liang, W., Nguyen, V. P., & Chen, Y. (2018). Experimental investigation of the effects of supercritical carbon dioxide on fracture toughness of bituminous coals. *International Journal of Rock Mechanics and Mining Sciences*, 107, 233–242. <https://doi.org/10.1016/j.ijrmm.2018.04.033>.
- Yu, Z., Liu, L., Yang, S., Li, S., & Yang, Y. (2012). An experimental study of CO₂-brine-rock interaction at in situ pressure-temperature reservoir conditions. *Chemical Geology*, 326–327, 88–101. <https://doi.org/10.1016/j.chemgeo.2012.07.030>.
- Zhang, K., Cheng, Y., Jin, K., Guo, H., Liu, Q., Dong, J., et al. (2017). Effects of supercritical CO₂ fluids on pore morphology of coal: Implications for CO₂ geological sequestration. *Energy & Fuels*, 31(5), 4731–4741.
- Zhang, D., Gu, L., Li, S., Lian, P., & Tao, J. (2013). Interactions of supercritical CO₂ with coal. *Energy & Fuels*, 27(1), 387–393.
- Zhang, Y., Lebedev, M., Al-Yaseri, A., Yu, H., Nwidee, L. N., Sarmadivaleh, M., et al. (2018a). Morphological evaluation of heterogeneous oolitic limestone under pressure and fluid flow using X-ray microtomography. *Journal of Applied Geophysics*, 150, 172–181.
- Zhang, Y., Lebedev, M., Sarmadivaleh, M., Barifcani, A., & Iglauer, S. (2016a). Swelling-induced changes in coal microstructure due to supercritical CO₂ injection. *Geophysical Research Letters*, 43(17), 9077–9083.
- Zhang, Y., Lebedev, M., Sarmadivaleh, M., Barifcani, A., Rahman, T., & Iglauer, S. (2016b). Swelling effect on coal microstructure and associated permeability reduction. *Fuel*, 182, 568–576.
- Zhang, G., Ranjith, P., Perera, M., Haque, A., Choi, X., & Sampath, K. (2018b). Characterization of coal porosity and permeability evolution by demineralisation using image processing techniques: A micro-computed tomography study. *Journal of Natural Gas Science and Engineering*, 56, 384–396.
- Zhang, X. G., Ranjith, P. G., Ranathunga, A. S., & Li, D. Y. (2019). Variation of mechanical properties of bituminous coal under CO₂ and H₂O saturation. *Journal of Natural Gas Science and Engineering*, 61, 158–168. <https://doi.org/10.1016/j.jngse.2018.11.010>.
- Zhang, Y., Xu, X., Lebedev, M., Sarmadivaleh, M., Barifcani, A., & Iglauer, S. (2016c). Multi-scale X-ray computed tomography analysis of coal microstructure and permeability changes as a function of effective stress. *International Journal of Coal Geology*, 165, 149–156.
- Zhou, S., Liu, D., Cai, Y., Yao, Y., & Li, Z. (2017). 3D characterization and quantitative evaluation of pore-fracture networks of two Chinese coals using FIB-SEM tomography. *International Journal of Coal Geology*, 174, 41–54.